Simultaneous Chandra X ray, Hubble Space Telescope ultraviolet, and Ulysses radio observations of Jupiter's aurora

R. F. Elsner,[1] N. Lugaz,[2] J. H. Waite Jr.,[2] T. E. Cravens,[3] G. R. Gladstone,[4] P. Ford,[5] D. Grodent,[6] A. Bhardwaj,[1,7] R. J. MacDowall,[8] M. D. Desch,[8] and T. Majeed[2]

Received 3 August 2004; revised 30 September 2004; accepted 5 November 2004; published 14 January 2005.

[1] Observations of Jupiter carried out by the Chandra Advanced CCD Imaging Spectrometer (ACIS-S) instrument over 24–26 February 2003 show that the auroral X-ray spectrum consists of line emission consistent with high-charge states of precipitating ions, and not a continuum as might be expected from bremsstrahlung. The part of the spectrum due to oxygen peaks around 650 eV, which indicates a high fraction of fully stripped oxygen in the precipitating ion flux. A combination of the OVIII emission lines at 653 eV and 774 eV, as well as the OVII emission lines at 561 eV and 666 eV, are evident in the measure auroral spectrum. There is also line emission at lower energies in the spectral region extending from 250 to 350 eV, which could be from sulfur and/or carbon. The Jovian auroral X-ray spectra are significantly different from the X-ray spectra of comets. The charge state distribution of the oxygen ions implied by the measured auroral X-ray spectra strongly suggests that independent of the source of the energetic ions, magnetospheric or solar wind, the ions have undergone additional acceleration. This spectral evidence for ion acceleration is also consistent with the relatively high intensities of the X rays compared with the available phase space density of the (unaccelerated) source populations of solar wind or magnetospheric ions at Jupiter, which are orders of magnitude too small to explain the observed emissions. The Chandra X-ray observations were executed simultaneously with observations at ultraviolet wavelengths by the Hubble Space Telescope and at radio wavelengths by the Ulysses spacecraft. These additional data sets suggest that the source of the X rays is magnetospheric in origin and that the precipitating particles are accelerated by strong field-aligned electric fields, which simultaneously create both the several-MeV energetic ion population and the relativistic electrons observed in situ by Ulysses that are correlated with ~40 min quasi-periodic radio outbursts.

Citation: Elsner, R. F., et al. (2005), Simultaneous Chandra X ray, Hubble Space Telescope ultraviolet, and Ulysses radio observations of Jupiter's aurora, *J. Geophys. Res.*, *110*, A01207, doi:10.1029/2004JA010717.

1. Introduction

[2] Jupiter is a powerful source of X rays within our solar system [*Bhardwaj et al.*, 2002]. Early observations revealed both a high-latitude source of X rays associated with Jupiter's aurora [*Metzger et al.*, 1983; *Waite et al.*, 1994] and a low-latitude source associated with particle precipitation from the radiation belts and/or scattered solar X rays [*Waite et al.*, 1997; *Maurellis et al.*, 2000]. More recent observations on 18 December 2000 [*Gladstone et al.*, 2002], using the Chandra X Ray Observatory's (CXO) High-Resolution Camera (HRC-I) instrument and the Hubble Space Telescope's Space Telescope Imaging Spectrograph (STIS) instrument, pinpointed most of the auroral X rays to a small high-latitude region that mapped along magnetic field lines into the outer Jovian magnetodisk at >30 Jovian radii from Jupiter. The northern auroral X-ray emissions observed with the HRC in December 2000 were tightly confined in longitude between 160 and 180 degrees S_{III} and in latitude between 60 and 70 degrees and thus were strongly correlated with the Jovian magnetic field.

[3] A surprising feature of the auroral X-ray light curve from the 18 December 2000 CXO observations [see *Gladstone et al.*, 2000, Figure 2, upper panel] was a significant 40-min oscillation in the north (and perhaps also in the south). However, the HRC counting statistics in the south did not permit determination of the relative phase of the oscillations in the north and south.

[1]NASA Marshall Space Flight Center, Huntsville, Alabama, USA.
[2]Department of Atmospheric, Oceanic, and Space Sciences, University of Michigan, Ann Arbor, Michigan, USA.
[3]Department of Physics and Astronomy, University of Kansas, Lawrence, Kansas, USA.
[4]Southwest Research Institute, San Antonio, Texas, USA.
[5]Center for Space Research, Massachusetts Institute of Technology, Cambridge, Massachusetts, USA.
[6]Institut d'Astrophysique et de Géophysique, Université de Liège, Liege, Belgium.
[7]On leave from Space Physics Laboratory, Vikram Sarabhai Space Centre, Trivandrum, India.
[8]NASA Goddard Space Flight Center, Greenbelt, Maryland, USA.

0148-0227/05/2004JA010717$09.00

Table 1. Jupiter Observation Log

Instrument[a]	OBSID	Configuration	Start Time[b]	Stop Time[b]	Exposure, s
Chandra ACIS-S	03726	—[c]	24 1559:13	25 0019:00	29,623
Chandra HRC-I	02519		25 0030:23	25 2014:19	70,727
Chandra ACIS-S	04418	—[c]	25 2326:15[d]	26 0808:23	30,934
HST STIS FUV-MAMA	o8k802010	F25SRF2 ACCUM	24 1803:42	24 1828:14	129.6
HST STIS FUV-MAMA	o8k802fvq	F25SRF2 TIME-TAG	24 1830:37	24 1835:37	300.0
HST STIS FUV-MAMA	o8k802q0q	F25SRF2 TIME-TAG	24 1932:44	24 1937:44	300.0
HST STIS FUV-MAMA	o8k802020	F25SRF2 ACCUM	24 1941:12	24 2005:44	129.6
HST STIS FUV-MAMA	o8k801010	F25SRF2 ACCUM	25 2252:24[e]	25 2303:06[e]	576.0
HST STIS FUV-MAMA	o8k801020	25MAMA ACCUM	25 2306:39[e]	25 2322:53[e]	864.0
HST STIS FUV-MAMA	o8k801pqq	F25SRF2 TIME-TAG	25 2327:48	25 2332:48	300.0
HST STIS FUV-MAMA	o8k801pvq	F25SRF2 TIME-TAG	26 0021:38	26 0026:38	300.0
HST STIS FUV-MAMA	o8k801030	25MAMA ACCUM	26 0032:38	26 0051:38	101.8
HST STIS FUV-MAMA	o8k801qbq	F25SRF2 TIME-TAG	26 0056:33	26 0101:33	300.0
HST STIS FUV-MAMA	o8k801qgq	F25SRF2 TIME-TAG	26 0157:41	26 0202:41	300.0
HST STIS FUV-MAMA	o8k801040	25MAMA ACCUM	26 0208:41	26 0224:55	864.0
HST STIS FUV-MAMA	o8k801050	F25SRF2 ACCUM	26 0228:28	26 0239:10	576.0

[a]ACIS, Advanced CCD Imaging Spectrometer; HRC-I, High-Resolution Camera; HST, Hubble Space Telescope; STIS, Space Telescope Imaging Spectrograph.
[b]Day of 2003 February hh:mm:ss UT.
[c]Data taken with single-event threshold of 42 (instead of nominal 20) and split-event threshold of 35 (instead of nominal 13), in order to minimize the effect of a "red leak" in the optical blocking filter (OBF).
[d]After removing the first 11.296 ks during which the planet overlapped its location in the second bias frame; see text for details.
[e]Times fall during the interval when the planet overlapped its location in the second bias frame; see text for details.

[4] Forty-minute oscillations have been seen before at Jupiter during the Ulysses outbound flyby in early 1992 with in situ measurements of energetic particles in the outer dusk magnetosphere and have been correlated with quasi-periodic radio bursts from Jupiter [*McKibben et al.*, 1993; *MacDowall et al.*, 1993; *Karanikola et al.*, 2004]. The energetic ions and ~16 MeV relativistic electrons were observed in February 1992 when Ulysses was at high jovimagnetic latitudes on field lines that likely connected to the Jovian (southern) polar cap. This can explain the large acceleration we infer from the energetic ion population responsible for the X rays and correlates well with the observed spatial location of the X-ray source region. We use new X-ray observations from Chandra to explore this hypothesis. *Branduardi-Raymont et al.* [2004] report on recent XMM-Newton X-ray observations of Jupiter.

2. New Chandra Observations

[5] The CXO observed Jupiter on 24–26 February 2003, for four rotations of the planet (approximately 40 hours), using both the Advanced CCD Imaging Spectrometer (ACIS) and the imager of the High-Resolution Camera (HRC-I). The Chandra observations were accompanied by five orbits of Hubble Space Telescope (HST) observations, using the Space Telescope Imaging Spectrograph (STIS) FUV-MAMA camera with the F25SRF2 and 25MAMA (clear) filters, in both ACCUM and TIME-TAG modes. Table 1 provides a log of these observations and Figure 1 shows a timeline of the observations. At the time of these observations, Jupiter was 5.32 AU from the Sun and moved from 4.4083 AU from the Earth at the beginning to 4.4205 AU at end of the observations, producing a tiny decrease in its projected equatorial radius from 22.361 to 22.299 arcsecond.

[6] During the two ACIS exposures, separated by the HRC-I exposure, the telescope focused the planet on the back-illuminated S3 CCD, in order to take advantage of this CCD's sensitivity to low-energy X rays. The ACIS data were taken using the standard ACIS frame time of 3.241 s. Although CXO does not track moving objects such as planets, no repointings were necessary during any of the individual CXO exposures due to the large ACIS-S and HRC-I fields of view. The HST observations were arranged so as to maximize the time spent with the northern auroral X-ray spot [*Gladstone et al.*, 2002] in the field of view.

[7] The response of the ACIS optical blocking filter has a local peak in its transmission near ~9000 Å (i.e., a "red leak") that can affect ACIS S3 observations of optically bright solar system objects and nearby bright late-type stars

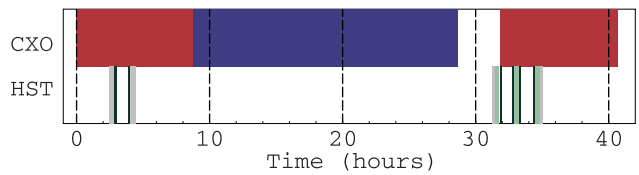

Figure 1. Bar chart showing the relative time sequence (in hours) of Chandra and Hubble Space Telescope (HST) observations of Jupiter during 24–26 February 2003. Chandra Advanced CCD Imaging Spectrometer (ACIS) S3 observations are in red, and HRC-I observations are in blue. The first 11.3 ks of the second ACIS exposure were removed because the planet overlapped its location in the second bias frame. Hubble Space Telescope Space Telescope Imaging Spectrograph (STIS) FUV-MAMA observations with the 25MAMA (clear) filter in ACCUM mode are shown in green, with the F25SRF2 filter in ACCUM mode in gray, and with the F25SRF2 filter in TIME-TAG mode in black. The first two HST datasets taken during the second ACIS exposure fall in the interval excised from the ACIS data.

[*Elsner et al.*, 2002]. Three steps were taken to reduce this problem to a manageable level for our Jupiter observations.

[8] First, the bias frame (normally used to determine the background and subtract it on board CXO) was taken with the planet off the S3 CCD during the first ACIS-S observation. This avoided the appearance of a brightness "bump" in the bias frame due to optical light from the bright planetary disk. Since the image of Jupiter moved across the detector during the ~8 hour ACIS observation, a normal bias image would have been worse than useless. Unfortunately, the planet remained in the field of view while taking the bias frame for the second ACIS observation, requiring us to excise the first 11.3 ks of data, during which the planet overlapped the bump in the bias frame. Two of the HST entries in Table 1 fell during this excised interval, as noted in footnote 4 to the table.

[9] Second, the single- and split-event thresholds for the ACIS S3 CCD were raised to 42 and 35, respectively (instead of the nominal values of 20 and 13), in order to avoid saturating the count rate with artificial X-ray events induced by the planet's bright optical emission.

[10] Third, the data were taken in Timed Exposure, Very Faint mode which records pulse-height-amplitudes in five-by-five pixel islands and permits a careful correction of the pulse-height-amplitude data for any residual optical effects using a specialized procedure developed by one of us (PGF). In this procedure, a local mean bias value is computed by averaging the 16 smallest pulse-height amplitudes from the 25 pixels of the event island. The appropriate bias frame values are added back into the amplitudes in the inner nine pixels and the local mean bias value subtracted. The data are then reprocessed using the standard CIAO tool *acis.process.events* in order to calculate corrected event grades, pulse-invariant channel values, and event energies. In our analysis, after applying this correction, we keep only the standard ASCA grades 0, 2, 3, 4, and 6. Owing to this necessary procedure, the single-pixel (grade 0) spectrum starts at ~100 eV, the two-pixel spectrum at ~168 eV, the three-pixel spectrum at ~236 eV, and the four-pixel spectrum at ~300 eV. There are very few five-pixel events. So for the spectral analysis we employ a low-energy cutoff at 300 eV (which made the distinction between carbon and sulfur lines in the observed spectra much harder) and use the standard response matrix for our spectral analyses, keeping in mind there may still be a tendency to undercount the higher grades (more pixel) events at the low end of our band. Charge-transfer-inefficiency (CTI) effects are minimal for the back-illuminated S3 CCD, and no CTI corrections were made.

[11] The ACIS S3 and HRC-I data were transformed into a frame of reference centered on Jupiter using appropriate ephemerides data obtained from the JPL HORIZONS program and Chandra orbit ancillary data provided in the data products from the Chandra X-ray Center (CXC).

[12] The ACIS-S 300–2000 eV count rate within a 1.05 Jupiter equatorial radius, averaged over both exposures, is 0.034 counts per second. The equivalent background count rate for events outside a 1.2 Jupiter equatorial radius, R_J, rescaled to a circle with radius 1.05 R_J, is 0.00088 counts per second, showing the effectiveness of Very Faint mode for suppressing background. In addition, the planet blocks X rays emitted from distant sources. Therefore for the ACIS data and the corresponding spectral analysis, we do not subtract background. The HRC-I count rate within a 1.05 R_J is 0.044 counts per second, while the equivalent background rate derived from a region outside 1.2 R_J is 0.014 counts per second. Cosmic rays and radioactive decay within the HRC-I's microchannel plate are the principal sources of HRC-I background and thus are not blocked by the planet. The equivalent rates for the 18 December 2000 HRC-I data were 0.080 counts per second within 1.05 R_J and 0.012 counts per second background. Thus the planet was significantly dimmer in X rays during the 24–26 February 2003 observations compared to the 18 December 2000 observations.

[13] For spectral modeling it is necessary to take account of the time-dependent contamination layer on the ACIS optical blocking filter [*Plucinsky et al.*, 2003]. We do this by multiplying the ACIS S3 effective area by an energy-dependent correction factor calculated using the CIAO tool *acisabs*. The resulting effective area curve is shown in the top panel of Figure 3 (see section 3). We also carry out the spectral analysis correcting for contamination by using the energy-dependent effective area correction factor calculated using the *contamarf* tool (H. L. Marshall, private communications, 2003). The spectral modeling results are indistinguishable using these two different contamination correction methods.

3. Spectral Analysis of the ACIS Data Set

[14] To analyze the spectral data the disk was divided, as shown in Figure 2, into three areas of interest: (1) the northern auroral zone, (2) the southern auroral zone, and (3) the disk (excluding the auroral zones). Following the preprocessing necessary for the spectral data described in section 2, spectral files, suitable for fitting in XSPEC [*Arnaud*, 1996] using the response and effective area files described above, were generated using LEXTRCT (A. F. Tennant, private communication, 2004). The measured X-ray spectra, which include the instrumental response, for the north and south auroral zones are shown in the middle two panels of Figure 3, where they can be compared with the ACIS-S effective area curve (top panel) and cometary X-ray spectra (bottom panel). The lower-latitude disk spectra will be described in a separate paper. The ACIS background rate derived from the 300–2000 eV events located outside 1.2 Jupiter radii and scaled to the area of the planetary disk is <3% of the emission from the total disk. In addition, the background contribution for true X rays from beyond Jupiter's orbit is blocked by the planet. As a result, we neglect the background in our spectral analysis of the ACIS data.

[15] We judge the acceptability of our spectral fits using the χ^2 statistic for an appropriate number of degrees of freedom ν (equal to the number of data points minus the number of fit parameters). Throughout this section we also provide the probability that statistical chance would yield an equivalent data set for which the same "fitting model" gives a χ^2 value greater than (i.e., a worse fit) the calculated/actual value. For example, for a value of χ^2 with a probability of 5%, we can reject the model-data fit that gave this value of χ^2 as unacceptable with, in this example, 95% confidence. On the other hand, the fit is statistically acceptable if this probability is sufficiently large. Reduced

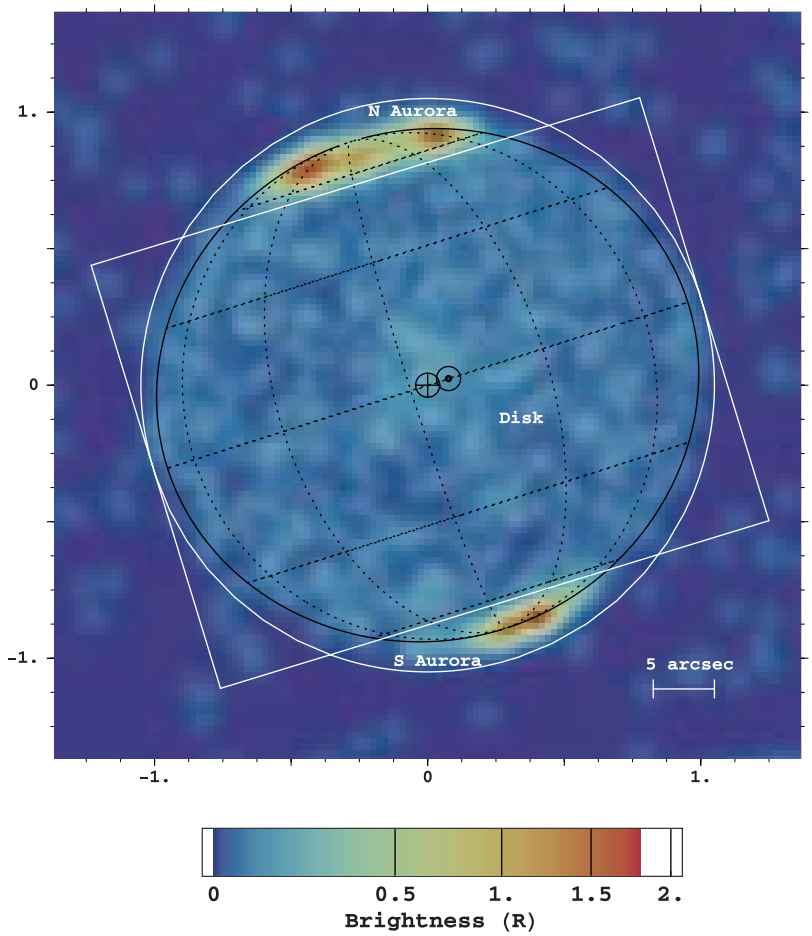

Figure 2. Color-coded image of ACIS-S (0.25–2.0 keV) events from 24–26 February 2003 observations as seen in a frame moving across the sky with Jupiter, smoothed with a two-dimensional gaussian with $\sigma = 0.738$ arcsec (1.5 ACIS pixel width). The white scale bar in the lower right represents 5 arcsec, and the small circles near the center represent the sub-Earth and subsolar points. The superimposed graticule shows latitude and longitude lines at intervals of 30°. For spectral analysis, north and south auroral events are defined as inside the white circle with radius 1.05 the Jovian equatorial radius and outside the white box, while disk events are defined as inside both the circle and the box. The total 0.25–2.0 keV count rate inside the dashed circle is 0.034 counts per second, while that within 0.75 Jovian radii but scaled to the size of the planet is 0.024 counts per second. The equivalent background rate derived from events more than 1.2 Jovian radii from the planet's center and scaled to the size of the planet is 0.00088 counts per second, showing the effectiveness of Very Faint mode for suppressing background. The color bar for the figure is in Rayleighs (R).

χ^2 is defined as the actual value of χ^2 divided by the number of degrees of freedom, ν. Reduced χ^2 has an expected mean value of unity, independent of the value of ν.

[16] The measured Jovian auroral X-ray spectra (middle two panels of Figure 3) have significant intensity levels in two energy bands: (1) 500–800 eV, presumably from oxygen transitions, and (2) 300–360 eV, probably from sulfur transition (although carbon transitions cannot be excluded, as will be discussed later in this section). The count rate in the 380–500 eV part of the auroral spectrum is relatively low. Emission also appears to exist below 300 eV, but we exclude this lower energy emission in our discussion due to concerns about the effect of our event regrading on the ACIS spectral response discussed earlier, see section 2. A comparison of the observed auroral spectra with the ACIS-S effective area curve (top panel of Figure 3) reveals some simple but important facts. The ACIS-S effective area curve exhibits a sharp drop at ~290 eV due to the presence of carbon in the optical blocking filter and absorption just above carbon K-edge at 284 eV. Above this edge the effective area rises relatively smoothly toward the oxygen K-edge at 532 eV. The relatively strong emission below 350 eV together with the corresponding deficit of X rays in the auroral spectrum over the 380–500 eV band are therefore inconsistent with a continuum spectrum, such as would be produced by a bremsstrahlung mechanism. We explicitly demonstrated this by fitting the thermal bremsstrahlung model available in XSPEC to the north auroral spectrum. The fitting parameters are the plasma temperature and a normalization; the model assumes cosmic abundances. Although the best-fit temperature value, ~250 eV, is in agreement with results from ROSAT PSPC

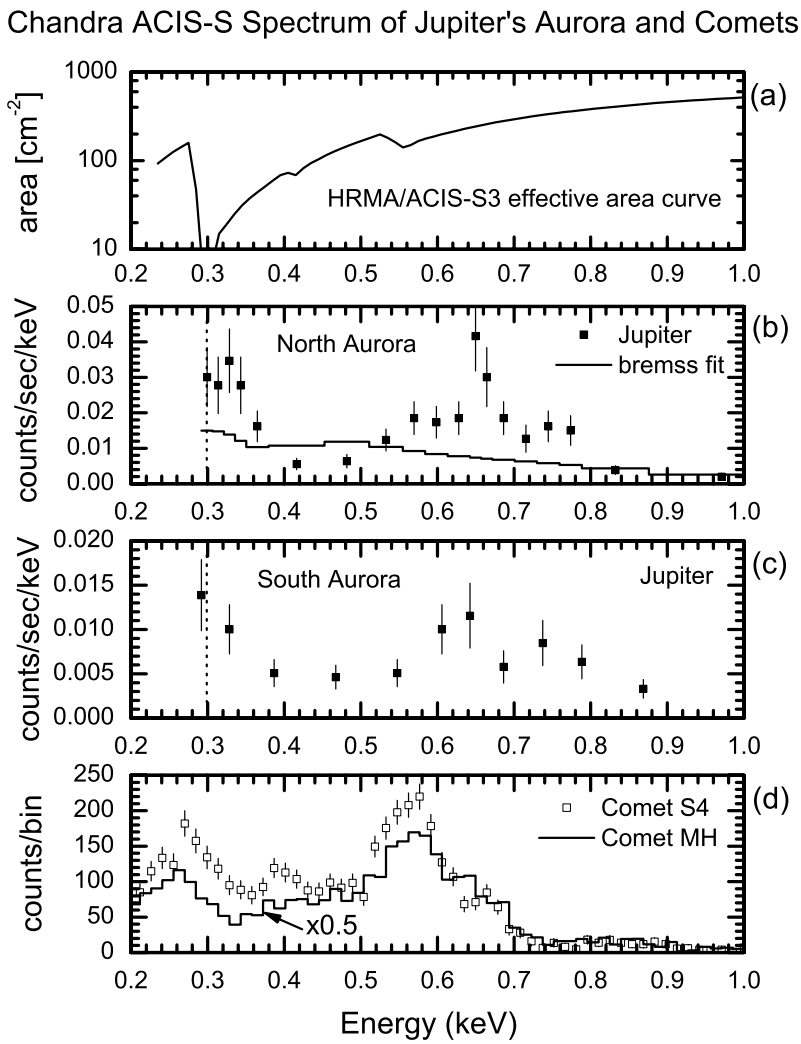

Figure 3. (a) ACIS-S effective area versus energy in kev, including the effects of contamination on the optical blocking filter at the time of the observations. (b) and (c) Jovian auroral X-ray spectra between 300 eV and 1 keV of the north auroral region (Figure 3b) and the south auroral region (Figure 3c) as defined in Figure 2, for the first ACIS-S observation. The vertical dotted line at 0.3 keV shows the low-energy cutoff for the Jovian spectra. Each spectral point represents $\geq$10 measured events. The solid line in Figure 3b shows the best-fit thermal bremsstrahlung model to the measured northern auroral spectrum. This result demonstrates that bremsstrahlung in particular, and probably any reasonable continuum model alone, cannot account for the observed spectrum. The lower global count as well as number of events of the south auroral zone compared to the north are clearly visible. (d) Chandra ACIS-S spectrums of comets Linear S4 [S4] and McNaught-Hartley [MH]; note that the spectrum for comet MH is plotted after scaling by a factor of 0.5. Two noticeable features present in Jovian spectra but absent (or very much weaker) in the cometary spectra are located at around 0.65 keV and 0.75 keV.

data [*Waite et al.*, 1994], the fit is extremely poor with a value for χ^2 of 91.1, a reduced χ^2 of 5.36, and a probability for chance occurrence greater than this value of 3.9×10^{-12}. This fit is shown with the data in the second panel of Figure 3. Comparison of the fit with the data suggests to us that no reasonable continuum model alone can hope to reproduce the shape of the measured spectrum. An electron bremsstrahlung mechanism is also very unlikely on energetic grounds [cf. *Bhardwaj and Gladstone*, 2000, and references therein].

[17] Line emission seems the more likely explanation for most of the observed auroral X-ray emission. Table 2 provides a list of possible lines from carbon, sulfur, and oxygen that are present in the 300–800 eV soft X-ray part of the spectrum. Oxygen lines from OVII (that is, O^{6+}) and OVIII (i.e., O^{7+}) are plausible candidates for the 500–

Table 2. Possible Sulfur, Carbon, and Oxygen Transitions in the 290–900 eV Region of the Auroral Spectrum

Energy, eV	Species/Charge State	Transition
299	CV	$1s2s \rightarrow 1s^2$
304–308	CV	$1s2p \rightarrow 1s^2$
314	SIX	$2p^3 4d \rightarrow 2p^4$ ($^3D \rightarrow {}^3P$)
316	SXI	$2p3d \rightarrow 2p^2$
336	SX	$2p^2 4d \rightarrow 2p^3$ ($^4P \rightarrow {}^4P$)
339–340	SXII	$3d \rightarrow 2p$ ($^2P \rightarrow {}^2P$)
348	SXIII	$3s \rightarrow 2p$
354	CV	$1s3p \rightarrow 1s^2$
367	CVI	$2p \rightarrow 1s$
371–378	CV	$1s4p, 5p \rightarrow 1s^2$
380	SXIV	$3s, 3d \rightarrow 2p$
435	CVI	$3p \rightarrow 1s$
459	CVI	$4p \rightarrow 1s$
561	OVII	$1s2s \rightarrow 1s^2$ ($^3S \rightarrow {}^1S$)
568	OVII	$1s2s \rightarrow 1s^2$ ($^3P \rightarrow {}^1S$)
574	OVII	$1s2p \rightarrow 1s^2$ ($^1P \rightarrow {}^1S$)
654	OVIII	$2p \rightarrow 1s$
665	OVII	$1s3p \rightarrow 1s^2$
698	OVII	$1s4p \rightarrow 1s^2$
713	OVII	$5p \rightarrow 1s$
774	OVIII	$3p \rightarrow 1s$
817	OVIII	$4p \rightarrow 1s$
836	OVIII	$5p \rightarrow 1s$

800 eV band emission. In particular, the broad emission peak near 650 eV could be due to OVIII lines. The emission in the lower energy band (300–360 eV) of the auroral spectrum could be due to either carbon or sulfur transitions. Carbon lines might suggest a solar wind source for the X-ray aurora, whereas sulfur would suggest a magnetospheric source. We now investigate these possibilities further by fitting simple model spectra to the observed spectra.

[18] We start with a simple 4-line fit to the spectrum for the northern auroral zone during the first ACIS observation. The lines were assumed to be Gaussians with fixed half-widths (σ) of 20 eV, and the best-fit line energies and total line fluxes are given in Table 3. This simple model fit gave a value for χ^2 of 7.33 for 10 degrees of freedom, a reduced χ^2 of 0.73, and a probability for chance occurrence greater than this value of 69.4%. In other words, this is an excellent fit. This simple model provides a handy numerical representation of the X-ray spectrum from Jupiter's northern auroral zone. Transitions from Table 2 with energies near the line energies in Table 3 include CV, SIX, and SX for the 313 eV line, OVII and OVIII for the 643 eV line, and OVIII for the 757 eV line. Table 2 does not include any transitions with line energies right near 539 eV, but there are OVII transitions close by at 560 eV. The X-ray luminosity or power emitted from the northern hot spot derived from this model is 0.68 GW.

[19] Next we consider more physically based fitting models. Powerful X-ray emission also originates within the solar system from comets (see the review by *Cravens* [2002]). The bottom panel of Figure 3 shows two cometary X-ray spectra measured by Chandra. The generally accepted explanation for cometary X-ray emission is the solar wind charge exchange (SWCX) mechanism. In this process, high charge-state heavy solar wind ions, (e.g., O^{7+}) acquire an electron from neutral atoms in the gas surrounding the comet's nucleus. The charge state of the solar wind ion is reduced (e.g., to O^{6+}), but the product ion is left in a highly excited state which then emits one or more soft X-ray photons [c.f. *Cravens*, 1997]. Recent CXO ACIS measurements have confirmed the likelihood of the SWCX model by finding the expected line emission features in the observed spectra [e.g., *Kharchenko et al.*, 2003; *Krasnopolsky et al.*, 2002; *Krasnopolsky*, 2004]. The measured cometary X-ray spectra for energies above 500 eV are dominated by the OVII helium-like lines near 560 eV, although lower intensity hydrogen-like lines from OVIII near 650 eV and 780 eV are also present (see Table 4 and Figure 5). We used the relative intensities given by *Kharchenko et al.* [2003] for a SWCX model to fit the Jovian spectrum. The results were not good – the fit was poor with a value for χ^2 of 55.0 for 10 degrees of freedom, a reduced χ^2 of 5.5, and a corresponding probability of this value or greater of 10^{-9}%. We also tried using the Kharchenko et al. spectrum but just for energies above 500 eV (i.e., the oxygen part of the spectrum) and found a reduced χ^2 of 2.16 and a probability of 1.1% (see Table 4). Evidently, the Jovian auroral spectrum has much less OVII line emission near 560 eV relative to the higher-energy OVIII lines in comparison with the cometary X-ray spectra. This can also been seen by a direct comparison of the ACIS-measured Jovian spectrum with ACIS-measured cometary spectra (compare Figure 3d with Figures 3b and 3c).

[20] We also fit the measured intensities with a range of collisional ionization equilibrium (CIE) models. We recognize that the physical excitation mechanism for the line emission is not the same in the aurora (presumably due to a combination of direct collisional excitation collisions and charge transfer collisions of the high charge-state precipitating ions species with atmospheric H_2) as it is in the CIE models (due to direct collisional ionization by hot electrons or as a by-product of dielectronic recombination), but the ionization states created and the specific lines excited should be the same and provide some insight into the source mechanism. We used the VAPEC model, which is incorporated in XSPEC [*Arnaud*, 1996] (available at http://heasarc.gsfc.nasa.gov/docs/xanadu/xspec/). This model is mainly used in the study of astrophysical plasmas, but it is based on the most-up-to-date line intensity data. Because each precipitating ion species might attain, during the acceleration process, a different mean energy because they could have different initial charge to mass ratios [*Cravens et al.*, 2003], we allowed each ion species to have its own temperature in our VAPEC collisional equilibrium model runs. We tried models with pure oxygen (for the higher energy band), with sulfur and oxygen, and with carbon and

Table 3. Best-Fit Parameters for a Simple Four Gaussian Line Model for the Northern Auroral Spectra

Line energy, eV	Total Line Flux, Photon/cm^2-s	Line Half-Width (σ), eV[a]
313	2.0×10^{-4}	20
539	7.2×10^{-6}	20
643	1.2×10^{-5}	20
757	4.7×10^{-6}	20

[a]Line half-widths fixed at 20 eV.

Table 4. Fit Parameters for the Spectral Region Between 500 and 900 eV for the Northern Auroral Spectra for Various Models of the Line Emission Ratios

Energy, eV	Cometary Charge Transfer Intensity-Kharchenko's	Fitted Intensity–Collisional Equilibrium Model with Free Charge-State Abundance	Transitions
560 ± 3	1	0.64	O^{6+} (n = 2 → 1) OVII $2\ ^{1,3}P \rightarrow 1\ ^{1}S$ OVII $2\ ^{3}S \rightarrow 1\ ^{1}S$
650 ± 6	0.35	1.08	O^{6+} (n = 3 → 1), OVII $3\ ^{1,3}P \rightarrow 1\ ^{1}S$ OVII $4\ ^{1}P \rightarrow 1\ ^{1}S$ O^{7+} (2p → 1s) OVIII $2\ ^{2}P \rightarrow 1\ ^{2}S$
780 ± 23	0.051	0.10	O^{7+} (3p,4p → 1s) OVIII $3,4\ ^{2}P \rightarrow 1\ ^{2}S$
845 ± 19	0.059	0.026	O^{7+} (4,5,6p → 1s) OVIII $5,6\ ^{2}P \rightarrow 1\ ^{2}S$

oxygen. The fit parameters are therefore the different plasma temperatures for the different species, the carbon or sulfur over oxygen ratio, and a normalization factor. We remind the reader that the temperature values derived below are not physical. Rather they are a representative parameterization for the ionization states probably responsible for the X-ray emission.

[21] Figures 4 and 5 show the data fits for the sulfur-oxygen and carbon-oxygen CIE models, respectively. Actually, two VAPEC models were run in each case (one for each species) and the results combined to fit the data. Both these fits were much more successful than the cometary model, mainly because the CIE models allowed a higher abundance of OVIII than OVII (due to the free oxygen temperature), whereas the OVIII to OVII ratio in the cometary model was not a free parameter and the cometary ratio is evidently not appropriate for the Jovian aurora. For the sulfur-oxygen plasma case (Figure 6), the value for χ^2 was 11.51 for 15 degrees of freedom, the reduced χ^2 was 0.7673, with a chance probability of a this value of χ^2 or greater being 71.6%. For the carbon-oxygen plasma case (Figure 7), the fit was significantly worse with a χ^2 of 23.6 for 15 degrees of freedom, a reduced χ^2 of 1.575, and a probability of 7.2%. These fit results indicate that a sulfur-oxygen "plasma" is more appropriate than a carbon-oxygen one as the source of the auroral X-ray

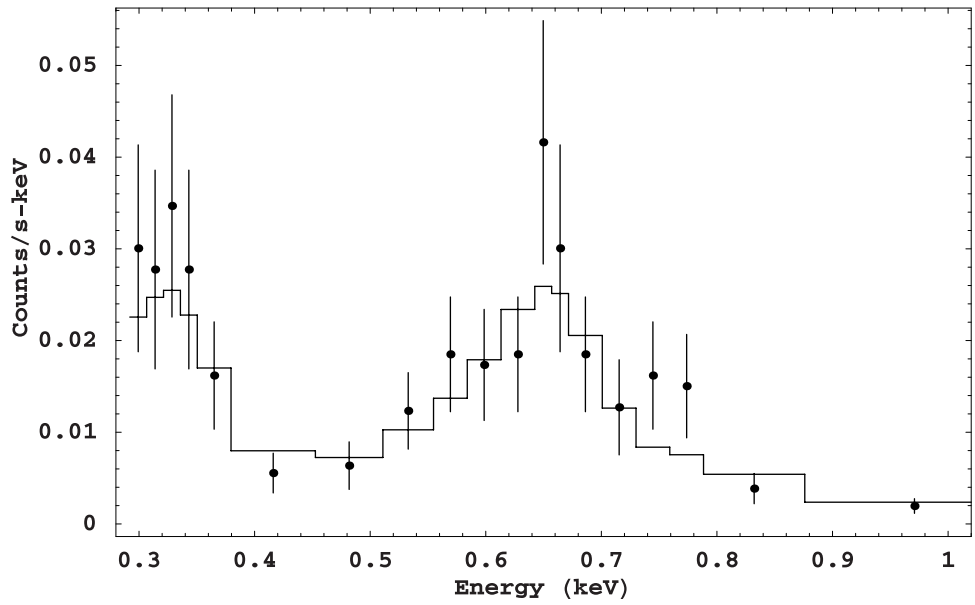

Figure 4. Fit with two added VAPEC models of the north auroral zone emission between 300 eV and 1 keV, for the first ACIS-S observation. The fitting parameters are the plasma temperatures of oxygen and sulfur, the ratio of sulfur over oxygen and a normalization factor. The VAPEC model assumes species are in collisional equilibrium. χ^2 is 11.51, the reduced χ^2 is 0.767, and the probability of chance occurrence of this value for χ^2 or greater is 71.6%. The S/O ratio is 16.6 times the solar value, the oxygen temperature is 355 eV, and the sulfur temperature is 172 eV.

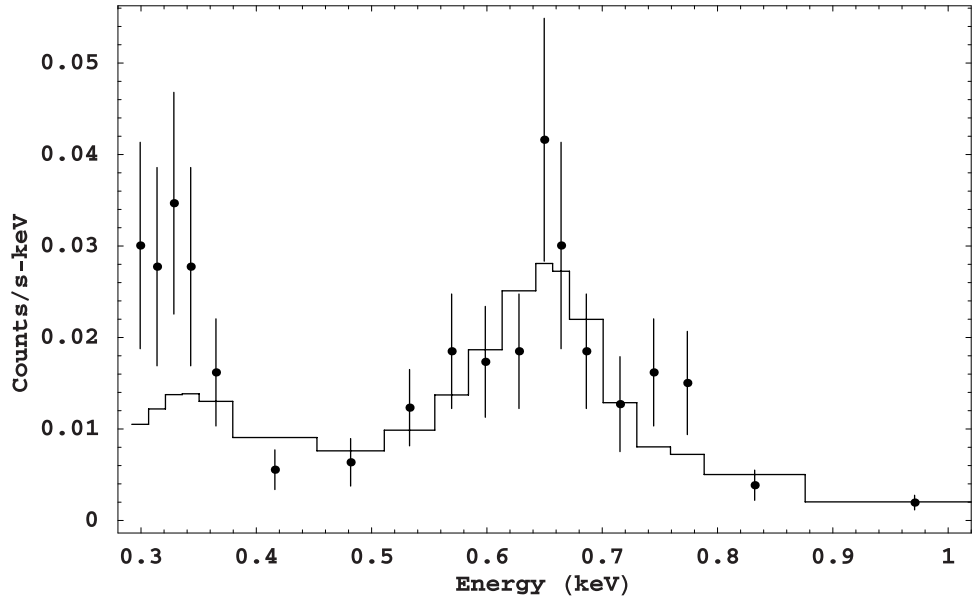

Figure 5. Fit with two added VAPEC models of the north auroral zone emission between 300 eV and 1 keV, for the first ACIS-S observation. The fitting parameters are the plasma temperatures of oxygen and carbon, the ratio of carbon over oxygen and a normalization factor. The VAPEC model assumes species that are in collisional equilibrium. The χ^2 is 23.6, the reduced χ^2 is 1.57, and the probability of this value of χ^2 or greater is 7.2%. The C/O ratio is 5.34 times the solar value, the oxygen temperature is 355 eV, and the carbon temperature is 81 eV.

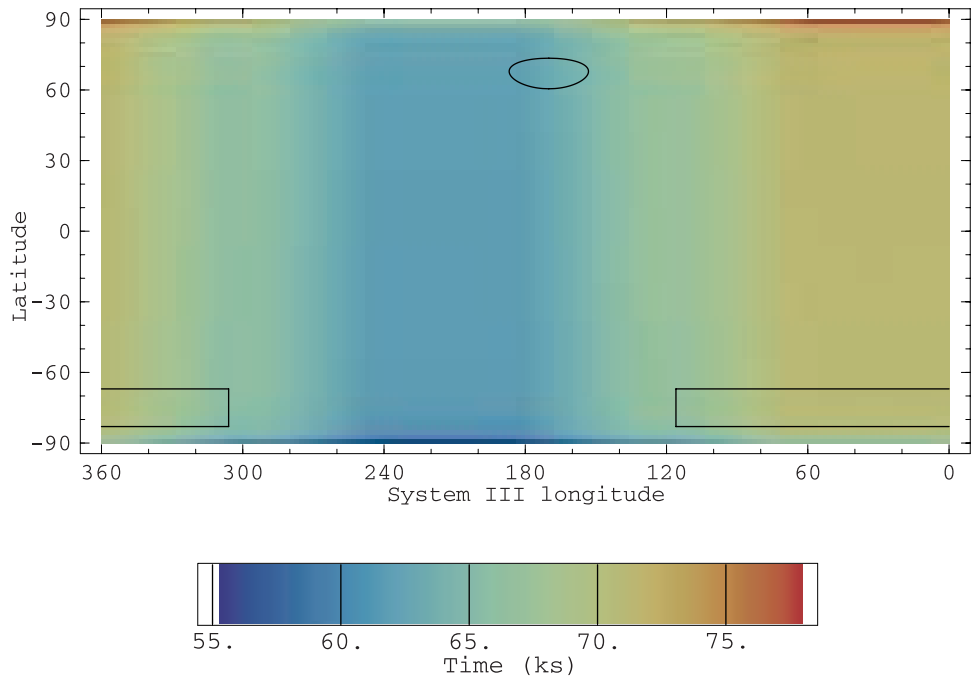

Figure 6. Exposure map for the 24–26 February 2003 data, summed over both ACIS-S exposures and the HRC-I exposure, in System III coordinates. The color scale was chosen to enhance contrast. The minimum and maximum exposure times are 55 ks and 78 ks, respectively, occurring at the very highest latitudes at the south and north poles. The exposure time varies by <16% over most of the map. The oval at top shows the region in the north, and the rectangle at the bottom shows the region in the south, used for timing analysis. The oval is defined as a circle (on the sphere) centered at 67°N latitude and 170° System III longitude with radius 6.5°. The rectangle lies between −67°S and −83°S latitude and 306°–360° and 0°–116° System III longitude. The color bar of the figure is in kiloseconds.

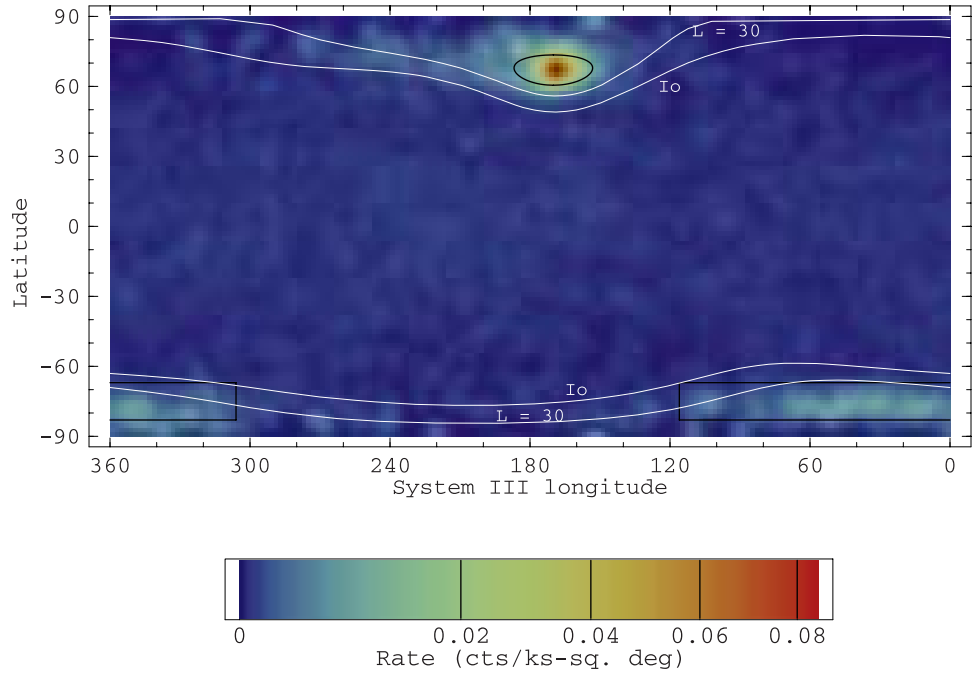

Figure 7. Rate map for the 24–26 February 2003 data, 250–2000 eV, summed over both ACIS-S exposures and the HRC-I exposure, in System III coordinates, convolved with a two-dimensional gaussian with $\sigma = 1.5°$. The lines crossing the plot from 360° to 0° trace the feet of the Io flux tube and the L = 30 flux tube, as defined by the VIP4 model, in the north and south hemispheres. The oval at top shows the region in the north, and the rectangle at the bottom the region in the south, used for timing analysis. The oval is defined as a circle (on the sphere) centered at 67°N latitude and 170° System III longitude with radius 6.5°. The rectangle lies between −67°S and −83°S latitude and 306°–360° and 0°–116° System III longitude. The color bar of the figure is in counts per kilosecond per square degree.

emission. In both cases, oxygen lines are used to fit the higher-energy part of the spectrum and there is little difference between the two cases. However, it appears that it is easier to fit the auroral intensity in the 300–400 eV part of the spectrum with sulfur lines than with carbon lines. These results favor a magnetospheric origin over a solar wind origin for the energetic particles presumed to be responsible for the X-ray aurora.

[22] The best-fit VAPEC model has an oxygen temperature of 355 eV and a sulfur temperature of 172 eV, roughly half the oxygen temperature. These fit temperatures arise from the charge state abundances in the CIE models which are needed to produce lines in the correct locations in the auroral spectrum, and these abundances depend on the temperature. The oxygen-sulfur temperature ratio is perhaps suggestive that the oxygen is accelerated to a higher energy than the sulfur (maybe due to a higher initial, preaccelerated, charge-to-mass ratio in the magnetosphere). However, because the CIE model does not have the correct physics for the Jovian aurora, verification of this supposition must await more appropriate physical models of the aurora.

[23] We now departed from the VAPEC model by allowing the charge state ratios to deviate from those in collisional equilibrium but constraining the relative line strengths within charge states to be those in collisional equilibrium. In these fits we kept the 3–5 strongest lines for each charge state. For the data above 500 eV, we obtained a reasonably good fit ($\chi^2 = 13.1$ for 9 degrees of freedom, reduced $\chi^2 = 1.457$, and a probability of 14.8%) with 48% OVIII and 52% OVII. An even better fit can be obtained by boosting the abundance of the high principal quantum number (i.e., n = 5–6) OVIII lines near an energy of 850 eV (see Tables 2 and 4) by a factor of 6 over the VAPEC model. In this case, we obtain a χ^2 of 10.1, a reduced χ^2 of 1.26, and a probability of 25.1% with the fit abundances of 42% OVIII and 58% OVII. What can we learn from the auroral spectrum at higher energies? Following arguments on charge state abundance versus beam energy using measured phase space densities for both solar wind and magnetospheric origins presented by *Cravens et al.* [2003], the presence of high principal quantum number OVIII lines argues for the acceleration of oxygen ions to energies above 1 MeV per nucleon. At these high energies, the incident oxygen ions are stripped of most of their electrons [*Cravens et al.*, 1995]. We will return to this in the discussion section.

[24] Now we further discuss the X-ray intensity between 300 eV and 500 eV. The intensity in the 360–500 eV band is low, whereas the measured 300–360 eV count rate is relatively high, especially considering the sharp drop in ACIS effective area just above 290 eV due to the carbon K-edge. Both carbon and sulfur ion species have transitions in the 300–360 eV band (see Table 2). Again, carbon would suggest a solar wind origin whereas sulfur would be consistent with a magnetospheric origin. Both C^{5+} and C^{6+} are abundant in the solar wind and the

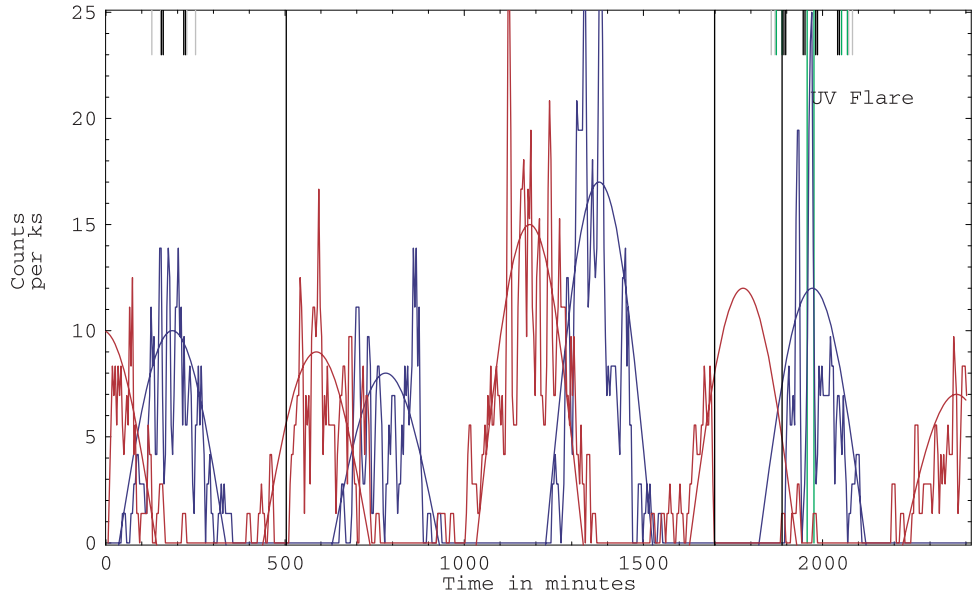

Figure 8. X ray count rate, in counts per kilosecond, for the northern (blue) and southern (red) auroral zones, created by 12-min boxcar smoothing of a 4-min binning of the data. The time origin corresponds to UT 1558:06 on 24 February 2003. The black vertical lines from top to bottom mark the transitions from ACIS-S to HRC-I exposures and back to ACIS-S. A gap appears at the beginning of the second ACIS-S exposure because we excised data taken when Jupiter overlapped its location in the second bias frame. The bars at the top mark the simultaneous HST observations, color-coded as in Figure 1. Note that the set of exposures containing the UV flare coincides with the tallest peak in the ACIS-S light curve for the northern auroral zone. Smooth sections of sine waves provide crude representations of projected area effects arising from the planet's rotation.

observed cometary X-ray spectrum is known to have CVI and CV soft X-ray lines due to the SWCX mechanism [cf. *Cravens*, 2002; *Kharchenko et al.*, 2003]. Carbon has also been detected in the Jovian magnetosphere [e.g., *Krimigis and Roelof*, 1983; *Lanzerotti et al.*, 1992], but its abundance is lower than that of oxygen and sulfur. Sulfur and oxygen are known to be very abundant in the Jovian magnetosphere, although the initial magnetospheric charge states are low (q = 1–3) in comparison with those needed to explain the X-ray observations. However, just as for oxygen, if magnetospheric carbon and sulfur ions are accelerated to sufficient energies, then higher charge states are produced by electron removal collisions upon impacting the Jovian atmosphere [cf. *Cravens et al.*, 1995]. Unfortunately, no detailed calculations have been undertaken for carbon and sulfur. Nonetheless, some inferences can be drawn from Table 2 and model fitting exercises to the observed spectrum.

[25] A pure sulfur model fit to the spectrum between 300 and 500 eV, allowing the charge state abundances to be fitting parameters but keeping the CIE relative line intensities gives a fit with χ^2 = 2.0 for 2 degrees of freedom, reduced χ^2 = 1.0, and a probability of 37.0%. The low count rate in this band leads to large errors but the best fit has a relative combined abundance of SX and SXI of 90–95% and 5–10% SXIV (ignoring all energies above 500 eV). A similar exercise for carbon gives a relative abundance of CV of about 96% with only 4% CVI. This large CV to CVI abundance ratio (required for a decent spectrum fit) presents a problem for either the solar wind or the magnetospheric mechanisms because the solar wind is known to have a high C^{6+} abundance, leading to CVI emission with the SWCX mechanism, and because for the magnetospheric case if most of the oxygen is O^{8+} or O^{7+}, then most of the carbon should be fully-stripped C^{6+}.

4. Timing Analysis

[26] Strong quasi-periodic oscillations on a timescale of ~45 min were clearly seen in the light curve and the power spectral density (PSD) for the X-rays from Jupiter's northern auroral zone observed with the HRC-I on 18 December 2000 [*Gladstone et al.*, 2002]. Quasi-periodic oscillations at a similar timescale are sometimes seen in the Ulysses radio data at 10s of kHz [*MacDowall et al.*, 1993; R. J. MacDowall, private communication, 2003].

[27] In order to search for such variations in the February 2003 Jupiter X-ray data, we first used the JPL Horizons ephemeris data to create an exposure map in System III coordinates (Figure 6). Except at the most extreme latitudes near the poles, the exposure time varies by <16% over most of the map, this variation being due to the gap in coverage introduced by removing the initial 11.3 ks from the second ACIS exposure.

[28] We then extracted X-ray events from regions in the northern and southern auroral zones. In System III coordinates (see Figure 7), the X-rays in the north are mostly confined to a hot spot, just as they were during the 18 December 2000 observations. In order to study their

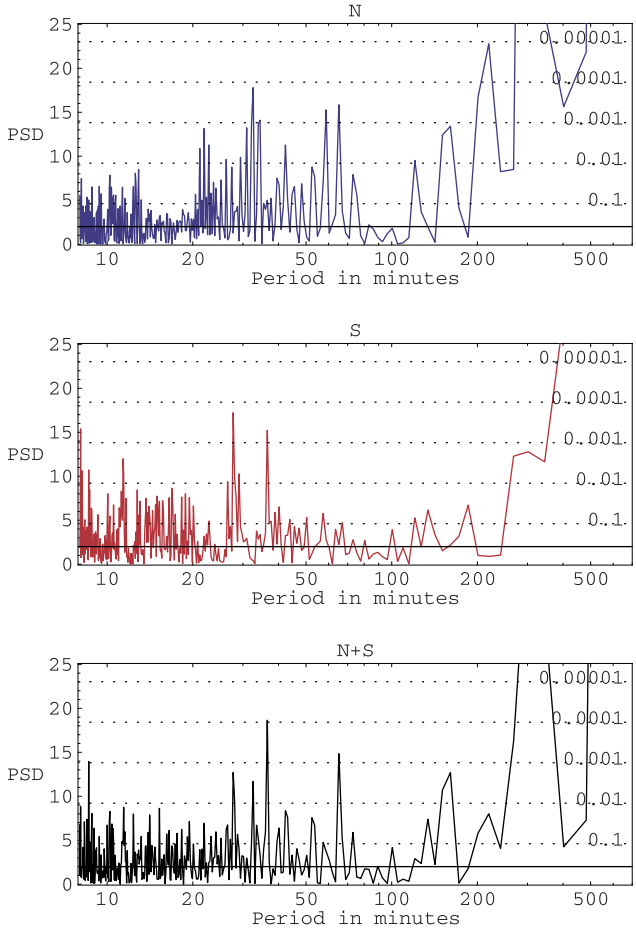

Figure 9. Power spectral density (PSD) versus period (in min), computed from the unsmoothed 4-min binning of the data for the northern (top), southern (middle), and sum of the northern and southern (bottom) auroral zones, respectively. In each plot, the solid line shows the expectation value for a steady source with Poisson statistics. The dotted lines show the single period probabilities of chance occurrence as labeled on the right. There are 217 independent periods between 10 and 100 min (301 in each complete PSD).

variability, we extracted events from a circle (in spherical coordinates) on Jupiter's surface centered at latitude 67°N and 170° system III longitude with radius 6.5°. Chandra's view of the southern polar regions was much better in February 2003 than it was in December 2000. The X-ray auroral emissions in the south appear confined to a band rather than a spot as in the north. For the south, we extracted events in the band between −83° and −67°S latitude and between 306° to 360° and 0° to 116° in System III longitude.

[29] The HRC-I and ACIS-S count rates are comparable (see section 2), so for the time-variability analysis we constructed time series including both ACIS-S exposures and the HRC-I exposure together. Since we are no longer concerned with preserving the ACIS-S spectral response, the ACIS-S data were restricted to the slightly expanded energy band 250–2000 eV. The HRC-I data include background, which is negligible for the ACIS-S data. The resulting time series for the northern and southern auroral zones are shown in Figure 8. The X-ray emission from the two zones as observed by CXO are clearly not simultaneous, with the peaks in the south displaced from those in the north by roughly 1/3 the planet's rotation period. However, in both zones the emission comes from those regions mapping to and beyond 30 R_J in the outer magnetosphere. Since we cannot follow these regions as they rotate around the planet, it remains possible that the apparent variations from each are correlated, which would indicate a common origin for both along the flux tube joining them. There are also clear variations in the peak intensity from cycle to cycle. There are 417 X-ray events in the light curve for the north and 397 X-ray events in the light curve for the south.

[30] In order to look for ~45 min oscillations, and any evidence for an additional link between the northern and southern auroral zones, we constructed three power spectral densities (PSD) for these data: (1) the northern light curve, (2) the southern light curve, and (3) the sum of the northern and southern light curves. These PSDs are shown in Figure 9 in the top, middle, and bottom panels, respectively. These PSDs were normalized, as suggested by *Leahy et al.* [1983], so that for Poisson-distributed data with sufficient counts, the dimensionless expectation value for the power at any frequency is two, and the distribution of power is χ^2 with two degrees of freedom. The dotted lines in the PSD plots show the single-frequency probabilities of chance occurrence, from bottom to top, of 0.1, 0.01, 0.001, 0.0001, and 0.00001, calculated from this distribution.

[31] All three PSDs show strong peaks related to Jupiter's rotation. None of them show evidence for quasi-periodic oscillations near 45 min, unlike the strong 45-min quasi-periodicity seen in the HRC-I observations in December 2000 [*Gladstone et al.*, 2002]. However, there are suggestive peaks in all three PSDs within the period range 10–100 min (containing 217 independent frequencies or periods). For each PSD, Table 5 lists the periods in this interval with single-frequency probabilities of chance occurrence <0.001. The significance levels quoted in the table take into account our search over 217 independent periods. These results may be marginal evidence of a more chaotic time variability on timescales more or less close to 45 min.

[32] In order to check whether the variation due to Jupiter's rotation and the gap in the second ACIS-S exposure introduce artifacts into these PSDs, we constructed a time series and PSD for all events outside the two auroral zones considered above (i.e., the disk X-ray emission). We found the PSD in the interval 10–100 min completely consistent with no significant time variability, as expected for emission most likely due to reflected and reprocessed solar X rays.

5. Comparison to Ulysses Radio Observations

[33] The Ulysses spacecraft is in a highly inclined, elliptical orbit with an aphelion of 5.4 AU, which sometimes places it less than a few AU from Jupiter. At these distances, the Ulysses radio receivers frequently observe

Table 5. Most Significant PSD Peaks

Region	Period, min	Significance, %
N + S	65.2	87.0
	36.5	98.1
N	65.2	92.1
	58.8	89.5
	34.5	81.1
	32.6	97.0
S	36.5	89.2
	27.7	96.0

Jovian radio emissions. The radio data described in this paper are a standard Ulysses data product binned to 144 s resolution; the plotted data are integrated over the frequency range 10 to 20 kHz.

[34] Ulysses radio data sometimes show ~40-min quasi-periodic oscillations (QP-40) in their PSDs, and sometimes the oscillations are clearly visible by eye in time history plots (R. J. MacDowall, private communication, 2003). One such example, from 6 October 2003, when Ulysses was 1.25 AU from Jupiter, is shown in Figure 10 (top left panel), where QP-40 are clearly seen. The QP-40 modulations are not the only variability seen in the radio and energetic electron and ion intensities seen by Ulysses in the Jovian high-latitude outer magnetosphere/magnetopause; variability also appears on timescales near 15, 30, 50, 60, and 80 min [*McKibben et al.*, 1993; *MacDowall et al.*, 1993; *Anagnostopoulos et al.*, 1998; *Marhavilas et al.*, 2001; *Karanikola et al.*, 2004]. The bottom left panel of Figure 10 shows the Ulysses radio data for the 3-day period 24–26 February 2003, containing the Chandra observation interval. At this time, Ulysses was 2.8 AU from Jupiter. The corresponding PSDs are shown in the right panels of Figure 10 (top, 6 October 2003; bottom, 24–26 February 2003). It is interesting to note that just like the X rays, the Ulysses radio data over the 3-day interval also show no evidence for strong quasi-periodic oscillations near 40–45 min. However, there is variability present in the Ulysses radio data at periods similar to that in the X-ray data (Figures 9 and 10 and Table 5). Also to be noted is that the significant peaks in the PSD for 6 October 2003 Ulysses data are not limited to 45 min.

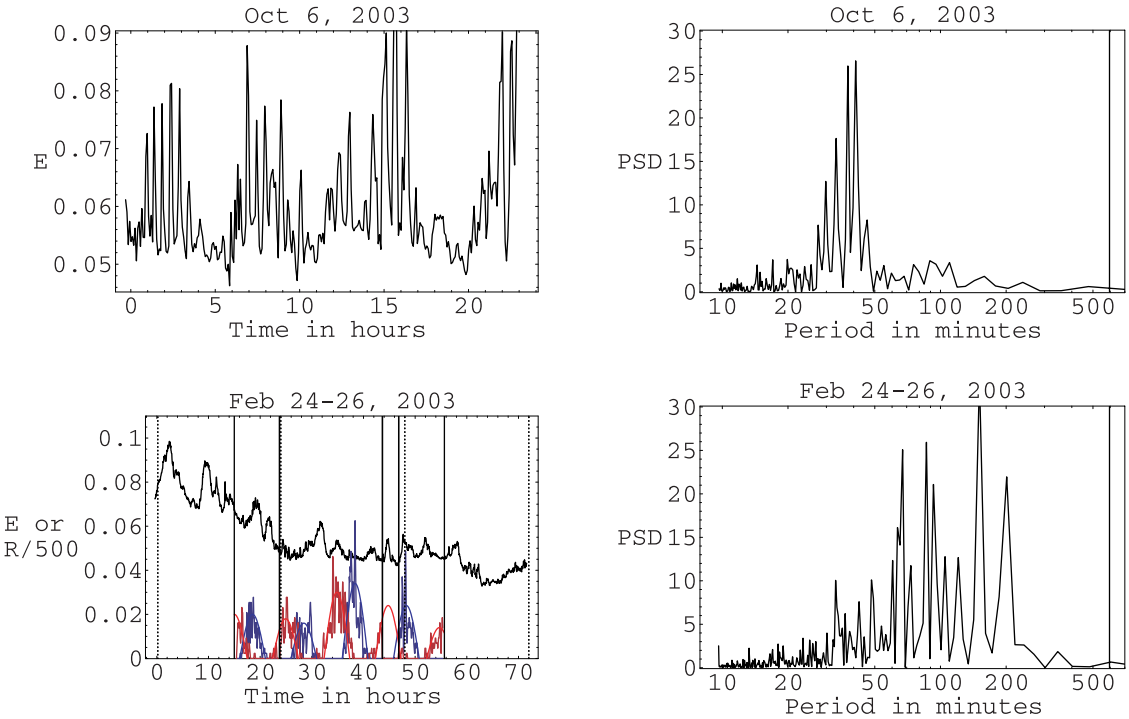

Figure 10. (top left) Time history for 6 October 2003 of Ulysses integrated electric field, 10–20 kHz, versus time in hours on 6 October 2003, clearly showing QP40 radio bursts. The data are averaged in 144 s bins. (bottom left) In black, the time history of the Ulysses integrated electric field, 10–20 kHz, versus time in hours on 24 February 2003, 0000:00, showing the data over a full 3-day interval. The data have been translated back in time from the spacecraft to Jupiter. The solid vertical lines mark the start (first ACIS-S, HRC-I, second ACIS-S) and the end (second ACIS-S) of the Chandra observations. The dotted vertical lines mark the start of each day (24–27 February 2003). Also shown are the Chandra count rates, R/500 where R is in counts per ks, versus time for the northern (blue) and southern (red) auroral zones. The Chandra data have also been translated back in time from the Earth to Jupiter (the light travel time across the Chandra orbit never exceeds 0.5 s). PSDs versus period in min for the Ulysses background subtracted data from (top right) 6 October 2003 and (bottom right) 24–26 February 2003. The solid vertical lines mark Jupiter's rotation period. Both PSDs show strong peaks, but that for 6 October 2003 is concentrated in a narrow band near 40 min, while that for 24–26 February 2003 is spread over a wider band above 30 min.

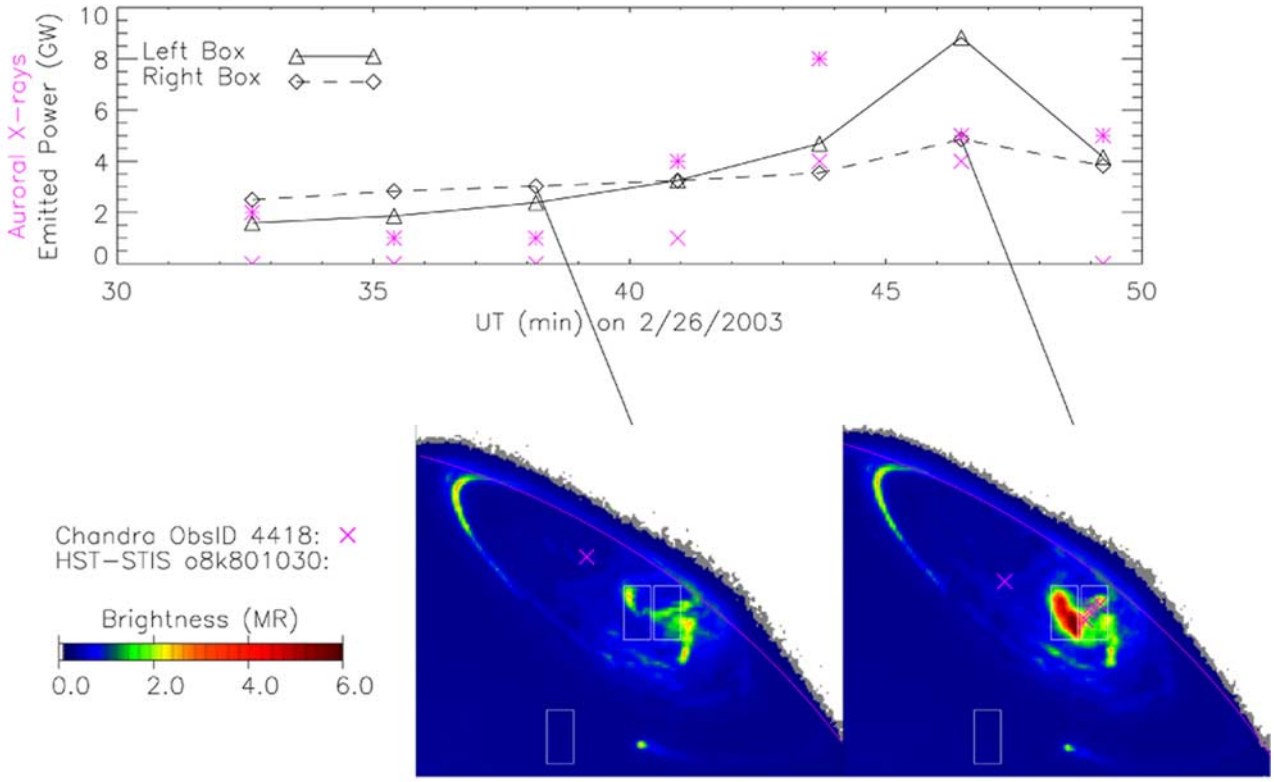

Figure 11. (top) FUV and X-ray light curves and (bottom) two HST-STIS image subframes showing a strong FUV flare in Jupiter's northern aurora observed on 26 February 2003. The FUV light curves are for the left and right subregions of the aurora shown in the HST-STIS images, while the X-ray light curve includes the entire aurora. Each HST-STIS image frame was exposed for 144 s using the FUV MAMA detector with no filter (CLEAR). Consecutive frames are separated by 22 s. The FUV flare appears to be mostly confined to the left box, while four out of five of the associated X rays (shown as pink crosses) appear in the box on the right. The isolated box at lower latitudes was used for FUV disk brightness subtraction. The average number of X ray counts per 144 s over a 2 hour span containing the flare is 1.3463; the rise in the number of X ray counts at the time of the FUV flare is statistically highly significant (see text). The FUV brightness scale is for all emitted FUV H_2 and H emissions (not just those in the STIS bandpass), before they are attenuated by the atmosphere (the atmospheric transmission was taken to be 0.4 below 130 nm); the conversion factor for these assumptions is 0.32 counts/s/pixel/MR.

[35] In order to further investigate whether there is any connection between the X-ray and radio emissions, we cross-correlated the mean subtracted X-ray event rate data with the background subtracted Ulysses radio data, using a time lag increment of 4.8 min, or 0.08 hours. It is somewhat surprising to us that no significant correlation was found, even when we broke the data into smaller segments that looked promising to the eye. However, the relatively small number of X-ray events per unit time limits the sensitivity of this analysis. We believe it would prove extremely instructive to compare simultaneous X-ray and radio observations taken at a time when the 40–45 quasi-periodic oscillations were strongly active in both wavelength bands.

6. Mapping the Source Region: Comparison With HST Observations at Ultraviolet Wavelengths

[36] HST observations were made concurrently with the Chandra observations, specifically to explore the relation of X-ray pulses [*Gladstone et al.*, 2002] relate to UV flares [cf. *Waite et al.*, 2001] seen from the same high-latitude auroral region. Fortunately, a strong FUV flare was observed to occur within the northern polar cap on 26 February 2003 at 0046 UT. The simultaneously acquired data sets are represented in the light curves shown in Figure 11. Also shown are two (out of seven in this sequence) sample ultraviolet image frames with X-ray events superimposed with pink colored crosses. The ultraviolet image frames showing the aurora are sequential 144 s frames, separated by 22 s gaps, obtained from HST STIS in ACCUM mode. The FUV light curve shows the development of an auroral flare. When the flare brightens the frequency of occurrence of the X-ray emissions in the hot spot also increases but not precisely in the maximum intensity region of the ultraviolet flare. The increase occurs on the dusk branch of the auroral oval that seems to be morphologically associated with the flare region in this image. The average number of 250–2000 eV counts per 144 s in the X-ray spot over a 2-hour span

containing the flare is $\lambda = 1.3464$, but the maximum number of X-ray counts per 144 s in that location during the flare is much higher at 7 counts. According to Poisson statistics, the chance probability of observing seven counts, as seen at the peak of the X-ray flare light curve, in a particular bin is only 0.04%. The fact that neighboring time bins also contain larger than average number of counts, in addition to the spatial association, increases the likelihood that this peak in the X-ray light curve is physically rather than coincidently related to the UV flare.

7. Discussion

[37] Several new characteristics of the Jovian X-ray aurora are evident in the new CXO observations reported in this paper: (1) the probable presence of high charge-state oxygen-line emission in the auroral X-ray spectra with line ratios which are distinctly different than those observed from comets; (2) the probable presence in the auroral spectra of high-charge state sulfur ions; (3) the existence of significant variability in the auroral X-ray flux but the absence of more regular ~45 min quasi-periodic variations seen in a previous CXO observation; (4) an apparent lack of correlation with the time history of simultaneous Ulysses radio observations (although this may only be the result of a lack of sensitivity due to the relatively small number of X-ray events) but similar periods of variability in both sets of power spectral densities (i.e., peaks in the 10–100 min range); and (5) a clear spatial and temporal association of the X-ray emission intensity with a Jovian auroral UV flare. What conclusions can be drawn from these various phenomena?

[38] *Cravens et al.* [2003] explored two scenarios thought to be plausible source mechanisms for the Jovian X-ray aurora: (1) highly charged solar wind heavy ions enter the magnetospheric cusp (on open field lines), are accelerated by a field-aligned potential, and then precipitate into the polar cap; and (2) heavy (e.g., S and O) ions in the outer magnetosphere (on closed field lines) are accelerated by a field-aligned potential and then precipitate in the high-latitude atmosphere. For the solar wind scenario, the heavy ions are already in high charge states (reflecting the wind's origin in the solar corona). The X rays are then produced in the same way that cometary X rays are [c.f. *Cravens*, 2002] through charge transfer collisions leading to highly excited product ions. For this scenario the acceleration is needed only to boost the ion flux high enough to explain the observed X-ray luminosity. For the magnetospheric scenario, energetic high charge state sulfur and oxygen ions produce X rays in the atmosphere via charge exchange collisions (and probably by direct excitation as well). However, the ions need to be accelerated to high energies in order that the original magnetospheric ions, which are known to exist in low charge states, undergo electron removal (i.e., stripping) collisions with atmospheric H_2, and thus become able to produce X rays. The parallel electric field postulated to cause this acceleration also enhances the ion flux. In order to obtain excited O^{6+} or O^{7+} ions via this precipitation process, the ions must be accelerated to estimated energies in excess of about 1 MeV/amu or total energies in excess of about 16 MeV [*Cravens et al.*, 1995; *Liu and Schultz*, 1999; *Kharchenko et al.*, 1998].

[39] Proton and helium ions are also accelerated by the potential and carry downward electrical current as well as produce ultraviolet emissions of their own. Downward electric current is also carried by upwardly accelerated secondary electrons produced by the primary ion precipitation. The accelerated secondary electrons might also be responsible for the quasi-periodic radio emission (i.e., QP-40 bursts), which have been observed from Jupiter and attributed to electron cyclotron maser emission [*MacDowall et al.*, 1993]. *Cravens et al.* [2003] estimated downward Birkeland currents of about 1000 MA were required for the solar wind case and about 10 MA for the magnetospheric case. In the solar wind case, the strong proton flux into the polar cap associated with such a large current would excite strong UV emission with a luminosity of $\sim 10^{14}$ W (including 300 kR of broadened Lyα from the precipitating protons alone), while even during the flare the observed flare UV emission reaches only $\sim 2 \times 10^{12}$ W and is much less at other times. For this paper, we carried out some simple calculations of energy deposition by 200 keV/amu heavy ion and proton precipitation followed by atmospheric transmission calculations at different photon energies. We found that the UV radiation (H Lyman α and H_2 Lyman and Werner bands) should almost all escape the atmosphere and be observable. On the basis of arguments like these, *Cravens et al.* [2003] concluded that the magnetospheric scenario was more likely than the solar wind scenario.

[40] The Chandra ACIS-S measured X-ray spectra presented in this paper, with their signatures of high charge states (particularly for oxygen), support an outer magnetosphere, or at least boundary layer, origin for the source population responsible for the X-ray aurora. The possible sulfur lines in the 300–350 eV portion of the spectrum also support a magnetospheric origin. However, without more detailed analysis and modeling, we cannot at this point entirely exclude the solar wind scenario. The charge states seen in the spectra, at least for oxygen, necessitate high incident energies, and hence require the existence of large field-aligned electric fields along the appropriate auroral magnetic field lines. OVIII emission features are more intense in the measured spectra than are the OVII features, suggesting that the incident ion beam has energies in excess of 16 MeV. Even for a very energetic beam it is surprising that the OVII 560 eV line(s) are as weak as they are, given that all charge states eventually are created in the cascading charge transfer process [*Cravens et al.*, 1995; *Liu and Schultz*, 1999; *Kharchenko et al.*, 1998]. Perhaps carbon transitions instead of, or in addition to, sulfur transitions can explain the 300–350 eV part of the spectrum, but in this case CV lines appear in the observed spectrum without significant emission from CVI transitions near 400–450 eV (for charge transfer excitation this would originate from fully stripped carbon). This seems unlikely given that at higher energies OVIII transitions (for charge transfer excitation this would originate from fully stripped oxygen) dominate over OVII transitions.

[41] The new CXO observations have thus established a probable magnetospheric, or at least boundary layer, origin for the energetic ions that evidently produce the auroral X rays. Given our knowledge of the ion populations in the outer magnetosphere [cf. *Mauk et al.*, 2002, 2004], this in turn requires that the ions undergo significant field-aligned

acceleration across a 10–20 MeV potential located a few Jovian radii above the poles [*Cravens et al.*, 2003]. Another implication is the existence of downward field-aligned currents of the order of 10 MA. Much of this current is thought to be carried by upwardly moving secondary electrons, which must then be accelerated to energies of 10–20 MV. This scenario is consistent with the Ulysses observations of ~16 MeV relativistic electrons flowing away from the planet in bursts with ~40 min periodicity [*McKibben et al.*, 1993]. The ~45 min quasi-periodicity previously observed by CXC [*Gladstone et al.*, 2002] strongly supports this scenario.

[42] Weaknesses of the solar wind precipitation X-ray emission mechanism include predicted large UV intensities (mainly from the associated proton precipitation), which has evidently not been observed, and predicted large field-aligned currents which are implausible in any reasonable solar wind-magnetosphere interaction scheme [e.g., *Bunce et al.*, 2004]. The magnetospheric ion precipitation mechanism does not suffer from those weaknesses. The proton to heavy ion ratio is much lower for the magnetospheric scenario than for the solar wind scenario so that this contribution to the UV intensities or to field-aligned currents is much less. Furthermore, we have carried out some simple calculations of energy deposition from ~16 MeV proton precipitation and found that most UV radiation at wavelengths less than 150 nm (this includes Lyman α) gets absorbed by the overlying atmosphere would not be seen externally by HST. However, X-ray emission from the heavy ion precipitation has no trouble escaping from the atmosphere.

[43] Although a formal cross-correlation analysis between the CXC X-ray and Ulysses radio data for 24–26 February 2003 does not show a significant relationship (possibly due to a lack of sensitivity caused by the relatively small number of X-ray events per unit time), it is true that strong quasi-periodic variability on a timescale of ~40 min is not present in either data set and that the PSDs for each dataset indicate variability on timescales in the range 20–70 min. In general, the Ulysses radio data show that the occurrence of quasi-periodic radio bursts have varying frequencies, as well as intervals when they are either multiperiodic, aperiodic, or nonexistent.

[44] The X-ray observations reported on in this paper combined with the interpretation presented by *Cravens et al.* [2003] supports the hypothesis that auroral X-ray emission is a diagnostic for downward field-aligned currents. The main auroral oval, observed in the UV, is thought to be due to upward currents carried by downwardly accelerated 100 keV electrons [*Grodent et al.*, 2001; *Gérard et al.*, 2003]. This Birkeland current connects to radially outward currents in the middle magnetosphere where the plasma begins to depart from corotation [cf. *Hill*, 2001; *Bunce and Cowley*, 2001; *Southwood and Kivelson*, 2001; *Cowley et al.*, 2003a, 2003b]. *Cowley et al.* [2003a, 2003b] suggested a picture in which, in addition to the current system associated with a departure from corotation (the subcorotating Hill region [*Hill*, 1979]), there is a solar wind-driven Dungey-type plasma convection and associated current system. At Earth, this directly driven Dungey-type convection and current system controls the aurora, but at Jupiter this system is squeezed into the outer part of the magnetosphere, which maps to part of the polar cap at the planet. This scenario also appears to be consistent with auroral infrared observations of Doppler-shifter H_3^+ in the auroral ionosphere [*Stallard et al.*, 2001]. *Grodent et al.* [2003] made a detailed comparison of the polar auroral UV emissions with the IR emissions reported by *Stallard et al.* [2003] in the light of recent plasma flow models [*Cowley et al.*, 2003a, 2003b].

[45] *Cravens et al.* [2003] suggested that the auroral X-ray emission is due to the return current portion of the main current system linking to the main auroral oval. Following this study, *Bunce et al.* [2004] suggested that the downward Birkeland current associated with the X-ray emission is not the return current but is due to pulsed reconnection near the dayside low-latitude magnetopause (under conditions of northward IMF). This region maps to the magnetic noon region just poleward of the main oval and is also where the UV active region [*Grodent et al.*, 2003], showing UV flares apparently associated with X-ray flares, is observed. They also suggested that pulsed reconnection could explain the time-dependence of the X-ray emission. *Bunce et al.* [2004] estimated field-aligned currents and voltages associated with this mechanism that, at least for a fast solar wind scenario, are consistent with the X-ray aurora characteristics discussed in *Cravens et al.* [2003]. Hence this cusp/magnetopause mechanism appears to be very promising. However, the X-ray emission data (in particular, where it maps into the magnetosphere), although it is adequate to locate it poleward of the main oval and near the UV active region, is not yet adequate to distinguish between downward return currents associated with the Vasyliunas cycle from downward currents associated with the Dungey cycle. However, it is clear that X-ray observations provide important quantitative constraints on our understanding of Jovian magnetospheric dynamics and the related magnetosphere-ionosphere coupling. It is hoped that further improvements in the X-ray observations, coupled with other observations, will allow auroral mechanisms, such as that proposed by *Bunce et al.* [2004], to be tested.

[46] **Acknowledgments.** We thank Vladimir Krasnopolsky for providing the cometary X-ray spectrum data shown in Figure 3c. A. Bhardwaj is supported by National Research Council Senior Resident Research Associateship at NASA-MSFC. D. Grodent is supported by the Belgian Fund for Scientific Research (FNRS). This research was supported in part by guest observer grants from the Chandra X-ray Center.

[47] Arthur Richmond thanks Vasili Kharchenko and another reviewer for their assistance in evaluating this paper.

References

Anagnostopoulos, G. C., P. K. Marhavilas, E. T. Sarris, I. Karanikola, and A. Balogh (1998), Energetic ion populations and periodicities near Jupiter, *J. Geophys. Res.*, *103*, 20,055–20,073.

Arnaud, K. A. (1996), XSPEC: The first ten years, in *Astronomical Data Analysis Software and Systems V, ASP Conf. Ser.*, vol. 101, edited by G. Jacoby and J. Barnes, p. 17, Astron. Soc. of the Pacific, San Francisco, Calif.

Bhardwaj, A., and G. R. Gladstone (2000), Auroral emissions of the giant planets, *Rev. Geophys.*, *38*, 295–353.

Bhardwaj, A., et al. (2002), Soft X-ray emissions from planets, moons, and comets, *ESA-SP-514*, pp. 215–226, Eur. Space Agency, Paris.

Branduardi-Raymont, G., R. F. Elsner, G. R. Gladstone, G. Ramsay, P. Rodriguez, R. Soria, and J. H. Waite Jr. (2004), First observation of Jupiter by XMM-Newton, *Astron. Astrophys.*, *424*, 331–337.

Bunce, E. J., and S. W. H. Cowley (2001), Divergence of the equatorial current the dawn sector of Jupiter's magnetosphere: Analysis of Pioneer Voyager magnetic field data, *Planet. Space Sci.*, *49*, 1089–1113.

Bunce, E. J., S. W. H. Cowley, and T. K. Yeoman (2004), Jovian cusp processes: Implications for the polar aurora, *J. Geophys. Res.*, *109*, A09S13, doi:10.1029/2003JA010280.

Cowley, S. W. H., E. J. Bunce, T. S. Stallard, and J. D. Nichols (2003a), Origins of Jupiter's main oval auroral emissions, *J. Geophys. Res.*, *108*(A4), 8002, doi:10.1029/2002JA009329.

Cowley, S. W. H., E. J. Bunce, T. S. Stallard, and S. Miller (2003b), Jupiter's polar ionospheric flows: Theoretical interpretation, *Geophys. Res. Lett.*, *30*(5), 1220, doi:10.1029/2002GL016030.

Cravens, T. E. (1997), Comet Hyakutake X-ray source: Charge transfer of solar wind heavy ions, *Geophys. Res. Lett.*, *24*, 105–108.

Cravens, T. E. (2002), X-ray emission from comets, *Science*, *296*, 1042–1045.

Cravens, T. E., E. Howell, J. H. Waite Jr., and G. R. Gladstone (1995), Auroral oxygen precipitation at Jupiter, *J. Geophys. Res.*, *100*, 17,153–17,161.

Cravens, T. E., J. H. Waite, T. I. Gombosi, N. Lugaz, G. R. Gladstone, B. H. Mauk, and R. J. MacDowall (2003), Implications of Jovian X-ray emission for magnetosphere-ionosphere coupling, *J. Geophys. Res.*, *108*(A12), 1465, doi:10.1029/2003JA010050.

Elsner, R. F., et al. (2002), Discovery of soft X-ray emission from Io, Europa, and the Io plasma torus, *Astrophys. J.*, *572*, 1077–1082.

Gérard, J.-C., J. Gustin, D. Grodent, J. T. Clarke, and A. Grard (2003), Spectral observations of transient features in the FUV Jovian polar aurora, *J. Geophys. Res.*, *108*(A8), 1319, doi:10.1029/2003JA009901.

Gladstone, G. R., et al. (2002), A pulsating auroral X-ray hot spot on Jupiter, *Nature*, *415*, 1000–1003.

Grodent, D., J. H. Waite Jr., and J.-C. Gérard (2001), A self consistent model of the Jovian auroral thermal structure, *J. Geophys. Res.*, *106*, 12,933–12,952.

Grodent, D., J. T. Clarke, J. H. Waite Jr., S. W. H. Cowley, J.-C. Gérard, and J. Kim (2003), Jupiter's polar auroral emissions, *J. Geophys. Res.*, *108*(A10), 1366, doi:10.1029/2003JA010017.

Hill, T. W. (1979), Inertial limit on corotation, *J. Geophys. Res.*, *84*, 6554.

Hill, T. W. (2001), The Jovian auroral oval, *J. Geophys. Res.*, *106*, 8101–8107.

Karanikola, I., M. Athanasiou, G. C. Anagnostopoulos, G. P. Pavlos, and P. Preka-Papadema (2004), Quasi-periodic emissions (15–80 min) from the poles of Jupiter as a principal source of the large-scale high-latitude magnetopause boundary layer of energetic particle, *Planet. Space Sci.*, *52*, 543–559.

Kharchenko, V., W. Liu, and A. Dalgarno (1998), X-ray and EUV emission spectra of oxygen ions precipitating into the Jovian atmosphere, *J. Geophys. Res.*, *103*, 26,687–26,698.

Kharchenko, V., M. Rigazio, A. Dalgarno, and V. A. Krasnopolsky (2003), Charge abundances of the solar wind ions inferred from cometary X-ray spectra, *Astrophys. J.*, *585*, L73–L75.

Krasnopolsky, V. A. (2004), Comparison of X-rays from comets LINEAR (C/1999 S4) and McNaught-Hartlet (C/1999 T1), *Icarus*, *167*, 417–423.

Krasnopolsky, V. A., D. J. Christian, V. Kharchenko, A. Dalgarno, S. J. Wolk, C. M. Lisse, and S. A. Stern (2002), X-ray emission from comet McNaught-Hartley, *Icarus*, *160*, 437–447.

Krimigis, S. M., and E. C. Roelof (1983), Low-energy particle population, in *Physics of the Jovian Magnetosphere*, edited by A. J. Dessler, pp. 106–156, Cambridge Univ. Press, New York.

Lanzerotti, L. J., T. P. Armstrong, R. E. Gold, K. A. Anderson, S. M. Krimigis, R. P. Lin, M. Pick, E. C. Roelof, E. T. Sarris, and G. M. Simnett (1992), The hot plasma environment at Jupiter—Ulysses results, *Science*, *257*, 1518–1524.

Leahy, D. A., W. Darbro, R. F. Elsner, M. C. Weisskopf, S. Kahn, P. G. Sutherland, and J. E. Grindlay (1983), On searches for pulsed emission with application to four globular cluster X-ray sources—NGC 1851, 6441, 6624, and 6712, *Astrophys. J.*, *266*, 160–170.

Liu, W., and D. R. Schultz (1999), Jovian X-ray aurora and energetic oxygen ion precipitation, *Astrophys. J.*, *526*, 538–543.

MacDowall, R. J., M. J. Kaiser, M. D. Desch, W. M. Farrell, R. A. Hess, and R. G. Stone (1993), Quasiperodic Jovian radio bursts: Observations from the Ulysses Radio and Plasma Wave Experiment, *Planet. Space Sci.*, *41*, 1059–1072.

Marhavilas, P. K., G. C. Anagnostopoulos, and E. T. Sarris (2001), Periodic signals in Ulysses' energetic particle events upstream and downstream from the Jovian bow shock, *Planet. Space Sci.*, *49*, 1031–1047.

Mauk, B. H., B. J. Anderson, and R. M. Thorne (2002), Magnetosphere-ionosphere coupling at Earth, Jupiter, and beyond, in *Atmospheres in the Solar System: Comparative Aeronomy*, *Geophys. Monogr. Ser.*, vol. 130, edited by M. Mendillo, A. F. Nagy, and J. H. Waite, pp. 97–114, AGU, Washington, D.C.

Mauk, B. H., D. G. Mitchell, R. W. McEntire, C. P. Paranicas, E. C. Roelof, D. J. Williams, and S. Krimigis (2004), Energetic ion characteristics and neutral gas interactions in Jupiter's magnetosphere, *J. Geophys. Res.*, *109*, A09S12, doi:10.1029/2003JA010270.

Maurellis, A. N., T. E. Cravens, G. R. Gladstone, J. H. Waite, and L. W. Acton (2000), Jovian X-ray emission from solar X-ray scattering, *Geophys. Res. Lett.*, *27*, 1339–1342.

McKibben, R. B., J. A. Simpson, and M. Zhang (1993), Impulsive bursts of relative electrons discovered during Ulysses traversal of Jupiter's dusk-side magnetosphere, *Planet. Space Sci.*, *41*, 1041–1058.

Metzger, A. E., D. A. Gilman, J. L. Luthey, K. C. Hurley, H. W. Schnopper, F. D. Seward, and J. D. Sullivan (1983), The detection of X-rays from Jupiter, *J. Geophys. Res.*, *88*, 7731–7741.

Plucinsky, P. P., et al. (2003), Flight spectral response of the ACIS instrument, in *X-Ray and Gamma-Ray Telescopes and Instruments for Astronomy*, edited by J. E. Truemper and H. D. Tananbaum, *Proc. SPIE*, *4851*, 89–100.

Southwood, D. J., and M. G. Kivelson (2001), A perspective on the influence of the solar wind on the Jovian magnetosphere, *J. Geophys. Res.*, *106*, 6123–6130.

Stallard, T., S. Miller, G. Millward, and R. D. Joseph (2001), On the dynamics of the Jovian ionosphere and thermosphere I. The measurement of ion winds, *Icarus*, 475–491.

Stallard, T. S., S. Miller, S. W. H. Cowley, and E. J. Bunce (2003), Jupiter's polar ionospheric flows: Measured intensity and velocity variations poleward of the main auroral oval, *Geophys. Res. Lett.*, *30*(5), 1221, doi:10.1029/2002GL016031.

Waite, J. H., Jr., F. Bagenal, F. Seward, C. Na, G. R. Gladstone, T. E. Cravens, K. C. Hurley, J. T. Clarke, R. Elsner, and S. A. Stern (1994), ROSAT observations of the Jupiter aurora, *J. Geophys. Res.*, *99*, 14,799–14,809.

Waite, J. H., G. R. Gladstone, W. S. Lewis, P. Drossart, T. E. Cravens, A. N. Maurellis, B. H. Mauk, and S. Miller (1997), Equatorial X-ray emissions: Implications for Jupiter's high exospheric temperatures, *Science*, *276*, 104–108.

Waite, J. H., Jr., et al. (2001), An auroral flare at Jupiter, *Nature*, *410*, 787–789.

A. Bhardwaj and R. F. Elsner, NASA Marshall Space Flight Center, SD 50, Huntsville, AL 35812, USA. (ron.elsner@nasa.gov)

T. E. Cravens, Department of Physics and Astronomy, University of Kansas, Lawrence, KS 66045, USA.

M. D. Desch and R. J. MacDowall, NASA Goddard Space Flight Center, Code 695, Greenbelt, MD 20771, USA.

P. Ford, Center for Space Research, Massachusetts Institute of Technology, 37-635, 70 Vassar St., Cambridge, MA 02139, USA.

G. R. Gladstone, Southwest Research Institute, 6220 Culebra Road, San Antonio, TX 78228-0510, USA.

D. Grodent, Institut d'Astrophysique et de Géophysique, Université de Liège, Allée du 6 Août, 17, Liege, B-4000, Belgium.

N. Lugaz, T. Majeed, and J. H. Waite Jr., Department of Atmospheric, Oceanic, and Space Sciences, University of Michigan, 2455 Hayward St., Ann Arbor, MI 48109-2143, USA.